Journal of Materials Chemistry C

ROYAL SOCIETY OF CHEMISTRY

PAPER

View Article Online
View Journal | View Issue

Cite this: J. Mater. Chem. C, 2025, 13, 11077

Improvement of the chemical and physical gas adsorption ability of poly(3-hexylthiophene) thin films by ultraviolet-ozone exposure†

Nahyeon Gu[a] and Yeong Don Park *[ab]

Organic semiconductors are emerging as replacements for inorganic semiconductors, which are too rigid and heavy to be utilized in next-generation devices such as electronic skins (e-skins). However, organic sensors display a lower reactivity and selectivity with target gases than inorganic semiconductor-based gas sensors. In particular, organic sensors face critical limitations in that they have low charge density and surface energy. To address these limitations, we applied ultraviolet-ozone (UV-O_3) treatment to modify the surface of poly(3-hexylthiophene) (P3HT) thin films with the aim of enhancing their gas-sensing performance. Among the gas sensor devices, the P3HT sensor treated with UV-O_3 for 30 s exhibited remarkable sensing characteristics, achieving a sensitivity of 1.5%/ppm and a limit of detection of 21.5 ppb for NO_2 gas. The UV-O_3 treatment induces two primary effects: oxidation of the polymer surface and etching of the polymer chains. These changes have a profound impact on the P3HT film's physical and chemical properties. The oxidation and chain scission of the P3HT film induced by UV-O_3 increased the hydrophilicity and free volume of the active layer. These modifications were observed to enhance the sensitivity and selectivity of the sensor toward NO_2 gas by improving the interaction between gas molecules and the permeability in the channel region.

Received 6th January 2025,
Accepted 26th April 2025

DOI: 10.1039/d5tc00053j

rsc.li/materials-c

Introduction

With the continuous advancement of material science, sensor technology, and wearable devices, electronic skin (e-skin) has emerged as a leading innovation in the electronics sector.[1–3] In addition, the rapid development of industry has led to serious environmental pollution, thus fostering a growing interest in medicinal solutions. Recent trends have indicated a surge in the adoption of e-skin for medical applications that enable remote patient monitoring and personalized medicine.[1,4–7] E-skin comprises electronic components that can detect touch, pressure, temperature, and other environmental factors.[6]

Among the various sensing functions, hazardous gas detection plays an important role in monitoring air quality by detecting specific chemicals or gas molecules and ensuring safety in industries or homes by immediately responding to disasters, such as fires, through the detection of toxic substances. It can also be used to detect physiological changes in gases released from the human body, facilitating early diagnosis of various diseases.[8,9] The flexible nature of e-skin requires the use of organic materials.[10] The applications of organic semiconductor materials such as conjugated polymers extend well beyond wearable devices such as e-skins, underscoring the dynamic growth of this field.[11–15] Conjugated polymers have strong potential as next-generation gas sensors owing to their flexibility and lightweight properties, surpassing conventional inorganic semiconductors in material design and cost efficiency.[16–21] Despite the numerous potential applications of conjugated polymers, the performance and reliability of polymer-based gas sensors remain limited.[22,23] This limitation arises from the low reactivity of hydrocarbon-based polymer chains with low surface energies and low surface areas.

Various methods have been studied to improve the performance of organic gas sensors for the detection of target gas molecules. An effective approach for enhancing the performance of gas sensors is to integrate conjugated polymers with porous inorganic materials for easy gas adsorption and desorption. In our previous study, conjugated polymers were blended with various inorganic materials, metal–organic frameworks, zeolites, porous carbon, and perovskites to improve gas sensor performance.[24–30] To increase the selectivity of the gas sensor, surface functional groups of the inorganic materials -another key factor- were introduced to interact only with the target analyte.[29,30] However, mixing inorganic materials uniformly is challenging due to their different surface energies

[a] Department of Energy and Chemical Engineering, Incheon National University, Incheon 22012, Republic of Korea. E-mail: gunah1@inu.ac.kr, ydpark@inu.ac.kr
[b] Innovation Center for Chemical Engineering, Incheon National University, Incheon 22012, Republic of Korea

† Electronic supplementary information (ESI) available. See DOI: https://doi.org/10.1039/d5tc00053j

from those of polymers, making it difficult to produce a homogeneous blend film with uniform sensing characteristics.

Herein, we present a systematic study of ultraviolet-ozone ($UV\text{-}O_3$) methods as a facile post-treatment method for controlling the chemical and physical properties of poly(3-hexylthiophene) (P3HT) chains. $UV\text{-}O_3$ treatment is a powerful technique that leads to oxidation and other chemical modifications of the surface of organic materials.[31–34] Post-treatment of $UV\text{-}O_3$ over just seconds to minutes makes it easier to modify the chemical and physical structures of the polymer. The chemical and physical structural changes in the P3HT film induced by $UV\text{-}O_3$ changed the charge carrier transport and gas adsorption properties, which were thoroughly investigated with respect to the $UV\text{-}O_3$ exposure time for various toxic gases. The chemical properties, chain structures, morphologies, and optical/electrical characteristics of the P3HT films treated with $UV\text{-}O_3$ were systematically studied.

Experiments

$UV\text{-}O_3$ exposure on P3HT thin films and OFET preparation

The p-type organic semiconductor P3HT (M_w = 58 kDa) was obtained from Rieke Metals, Inc., and was used without further purification. Organic field-effect transistors (OFETs) were fabricated in a top-contact, bottom-gate (BGTC) structure using a highly n-doped silicon wafer as both the substrate and gate electrode. A thermally grown silicon dioxide (SiO_2) layer, with a thickness of 3000 Å, was employed as the gate dielectric. The substrate surface was cleaned by sonication in acetone and ethanol for 30 min each to remove organic impurities. Surface modification of the silicon wafer was then performed using hexamethyldisilazane (HMDS) *via* spin-coating at 2500 rpm for 30 s. P3HT was dissolved in chloroform at a concentration of 5 mg mL^{-1} and stirred at 50 °C for 2 h. The solution was deposited onto the substrate once it cooled to room temperature (25 °C). The P3HT solution was spin-coated onto the HMDS-treated SiO_2/Si substrates at 2500 rpm for 60 s at room temperature. The spin-coated P3HT films were treated with $UV\text{-}O_3$ for various durations (0, 5, 10, 30, and 60 s) using a $UV\text{-}O_3$ cleaner, which emitted UV wavelengths of 184.9 and 253.7 nm at an energy density of 33.3 mW cm^{-2}.

To fabricate BGTC-type OFET based on the P3HT thin films, Au electrodes (≈40 nm thick) were thermally evaporated through a metal shadow mask to form the source and drain electrodes. A square-patterned shadow mask with channel length and width of 100 and 2000 μm, respectively, was employed to pattern the Au electrodes, creating source and drain structures for OFET-based gas sensors. Fig. S1a (ESI†) displays a photograph of the OFET type gas sensor. For the ultraviolet-visible (UV-Vis) absorption measurements, identical P3HT films were deposited on transparent glass substrates using the same process applied to the silicon substrates.

Characterization

The surface morphologies of the P3HT films were investigated using atomic force microscopy (AFM, Multimode 8, Bruker) and a contact angle meter (phoenix-MT). The UV-Vis absorption spectra of the films were obtained using a Lambda 365 UV-Vis spectrophotometer (PerkinElmer) to study their molecular order and conjugated length. X-ray photoelectron spectroscopy (XPS, PHI 5000 Versa Probe II) was used to analyze the surface elements of the films, with all peaks calibrated to the C 1s peak at a binding energy of 285 eV. The electrical properties of the OFETs were characterized in a vacuum at room temperature using a semiconductor analyzer (Keithley 4200-SCS), and the drain current and field-effect mobility were measured. The P3HT films exposed to humidity were examined after storage in dark and ambient conditions (RH ≈ 30%) for a defined period. Furthermore, the sensing capabilities of the gas sensor devices were tested at room temperature using a precision sensor system (GASENTEST), with both gate and drain voltages set at −10 V. In the pulse-cycle sensing tests, the gas concentration was maintained at 10 ppm, whereas in the dynamic-cycle tests for NO_2, CO_2, and SO_2 gases, the concentration varied between 10 and 70 ppm. All the gases were supplied using calibrated gas cylinders containing an air mixture. Fig. S1b (ESI†) displays a photograph of the gas sensor performance test system.

Results and discussion

Chemical and physical structures of P3HT film

The effect of the $UV\text{-}O_3$ treatment on the surface morphology of the P3HT films was investigated using AFM. Fig. 1a presents the AFM height images, phase images, and corresponding root-mean-square roughness (R_q) values for the P3HT films subjected to various $UV\text{-}O_3$ exposure times. Initially, the untreated P3HT film (0 s) exhibited a surface R_q value of 0.94 nm, indicative of the intrinsic P3HT morphology characterized by the formation of partially distinct fibrillar structures, as evidenced by the phase image.

After 5 s of $UV\text{-}O_3$ exposure, the R_q value decreased to 0.75 nm, suggesting an initial surface smoothing, possibly due to the partial removal of loosely bound polymer chains. Further exposure to $UV\text{-}O_3$ for 10 and 30 s resulted in R_q values of 0.72 and 0.70 nm, respectively, indicating a gradual reduction in surface roughness. This trend continued with 60 s of $UV\text{-}O_3$ exposure, where the R_q value reached 0.66 nm, representing an ultra-smooth surface morphology. These results suggest that the $UV\text{-}O_3$ treatment effectively etched the P3HT surface, leading to the removal of superficial polymer layers and a reduction in surface roughness (Fig. 1b).

The hydrophilicity of the P3HT films was assessed by measuring the water contact angle (WCA) after various $UV\text{-}O_3$ exposure times (Fig. 1c). The initial WCA of the untreated P3HT film was 95.1°, reflecting the inherent hydrophobic nature of the P3HT surface due to the hydrocarbon chains. After 5 s of $UV\text{-}O_3$ treatment, the WCA remained largely unchanged at 95.0°, indicating a minimal alteration in the surface chemistry within this brief exposure period. However, as the exposure time increased to 10 s, a noticeable decrease in the WCA to

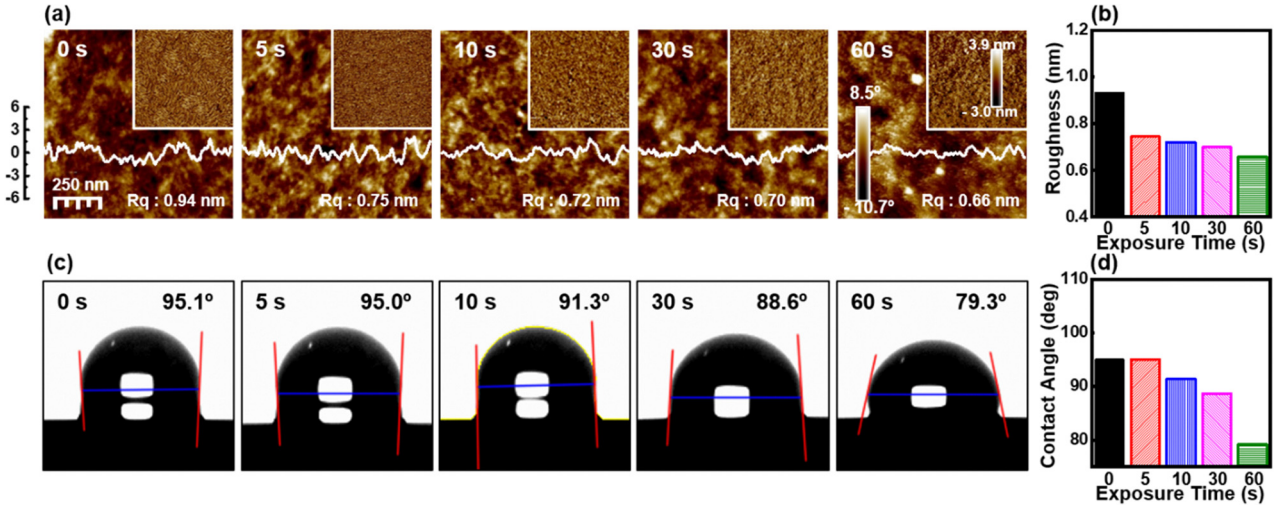

Fig. 1 (a) Height image, mean square roughness (R_q), and phase image (inset) of the P3HT films surface by AFM. (b) Summary of mean square roughness change by UV-O_3 exposure time. (c) Water contact angle of P3HT films. (d) Summary of water contact angle change by UV-O_3 exposure time.

91.3° was observed, suggesting the initiation of oxidative processes that introduced hydrophilic functional groups, such as hydroxyl or carbonyl groups, on the polymer surface. Continued exposure for 30 and 60 s led to further reductions in WCA to 88.6° and 79.3°, respectively. This progressive decrease in the WCA confirms the increased hydrophilicity of the P3HT surface with prolonged UV-O_3 exposure (Fig. 1d). The enhanced hydrophilicity is attributed to the oxidation of the P3HT chains and the introduction of polar groups, which increases the surface energy of the P3HT film.

The impact of the UV-O_3 treatment on the molecular order and conjugated length of the P3HT films was investigated using UV-Vis absorption spectroscopy (Fig. 2a–d). Fig. 2a shows the UV-Vis absorption spectra of the P3HT films subjected to varying durations of UV-O_3 exposure. The UV-Vis spectra exhibited characteristic absorption bands, corresponding to the electronic transitions in P3HT, with notable peaks at the (0-0) and (0-2) transitions. Brown *et al.* demonstrated that the latter structure can be assigned to interchain absorption from highly ordered domains.[35] The intensity of this signal depends on the regioregularity of the polymer and the packing of the P3HT chains. As the UV-O_3 exposure time increased, a progressive decrease in the overall spectral intensity was observed, particularly in the region corresponding to the π–π* (0-2) transition. This decrease in the absorption intensity can be attributed to the partial decomposition of the polymer chains, likely due to

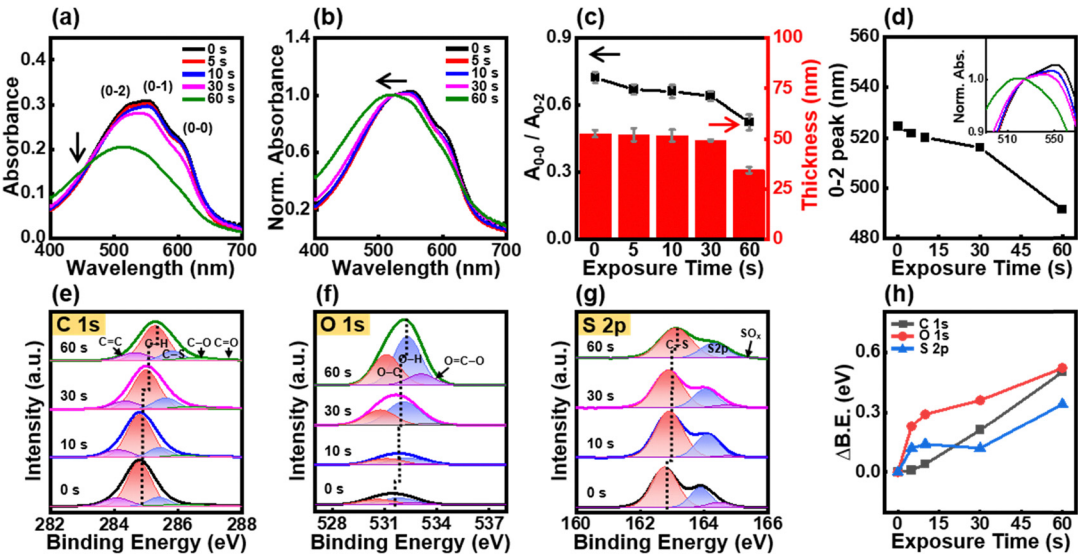

Fig. 2 (a) UV-Vis adsorption spectra and (b) UV-Vis adsorption normalized to (0-2) signal of P3HT film at various UV-O_3 exposure time. (c) Thickness (right axis) and intensity of (0-0) and (0-2) transitions (left axis). (d) Summary of (0-2) peak shift of P3HT film with the UV-O_3 exposure time. Inset shows the (0-2) peak shift in enlarged UV-Vis adsorption spectra. XPS spectra of P3HT film: (e) C 1s, (f) O 1s, and (g) S 2p. (h) Summary of binding energy change of P3HT film with the UV-O_3 exposure time.

the oxidative etching process induced by UV-O_3. The gradual reduction in the P3HT film thickness, as shown in Fig. 2c (right axis), further supports this observation. The reduction in thickness from 60 nm (untreated) to approximately 45 nm after 60 s of UV-O_3 exposure suggests the removal of the material from the surface. Additionally, the normalized absorption spectra in Fig. 2b reveal a shift in the (0-2) transition peak, indicating a change in the molecular ordering or conjugation length within the P3HT film. This shift is quantitatively summarized in Fig. 2d, where a systematic blue shift in the (0-2) peak is observed with increasing UV-O_3 treatment time, suggesting a reduction in the conjugation length due to chain scission.

The chemical compositions and oxidation states of the P3HT films after UV-O_3 treatments were analyzed using XPS. Fig. 2e–g display high-resolution XPS spectra of the C 1s, O 1s, and S 2p regions, respectively. The C 1s spectrum shows characteristic peaks corresponding to the C–C, C–S, and C–O bonds (Fig. 2e). As the exposure time increased, the C 1s size decreased, which indicated scission of the P3HT chains and a decrease in carbon density, as seen in the UV-Vis spectra. With increasing UV-O_3 exposure time, a shift toward higher binding energies was observed for all these components, indicating an increase in the oxidation state of carbon owing to the introduction of oxygen-containing groups. Similarly, the O 1s spectrum displayed a prominent peak associated with the O–C and O–H bonds (Fig. 2f). The intensity of the O–C peak increased with prolonged UV-O_3 treatment, suggesting the formation of more oxygenated species as the oxidation progressed. The S 2p spectrum showed peaks corresponding to C–S and S–S bonds (Fig. 2g). Similar to the C 1s spectrum, the S 2p peaks shifted to higher binding energies, which is consistent with the oxidation of sulfur atoms in the thiophene rings of P3HT. Several studies have reported the photooxidation and ozonation mechanisms of polymers, including P3HT.[36–40] According to these studies, with UV-O_3 treatment, oxidation occurs in both the backbone and the side chains of P3HT. This can be confirmed by the fact that not only C–C and C–H bonds but also bonds containing S in the backbone result in the formation of new bonds. A summary of the binding energy shifts for C 1s, O 1s, and S 2p as a function of the UV-O_3 exposure time is presented in Fig. 2h. These shifts reflect the progressive oxidation of the P3HT films, resulting in the cleavage of the existing C–C and C–S bonds and the formation of new C–O and S–O bonds.

The increase in oxygen content and the formation of an oxidized layer on the surface of the P3HT film are key indicators of oxidative degradation induced by UV-O_3 treatment. The observed decrease in the UV-Vis absorption intensity and shifts in the XPS binding energies can be correlated with the chemical modifications induced by UV-O_3. As the P3HT chains are oxidized, the conjugation length of the P3HT molecules decreases, leading to a blue shift in the absorption spectrum. Concurrently, chain scission, as revealed by XPS, contributes to the overall reduction in the carbon density owing to the breakdown of the conjugated backbone. These findings imply a dual role of the UV-O_3 treatment in increasing the free volume through etching and modifying the chemical structure through oxidation.

OFET performance

The electrical characteristics of the OFETs were analyzed at various UV-O_3 exposure times. Compared with the pristine P3HT film, the transfer curve shifted to the left and the drain current decreased with increasing UV-O_3 exposure time (Fig. 3a–c). The leftward shift indicates that the threshold voltage has shifted to a higher value. As the time of UV-O_3 treatment increased, the amount of the oxidation layer increased, resulting in a threshold voltage shift from −1 V to −18 V (Fig. 3b). The free volume formation caused

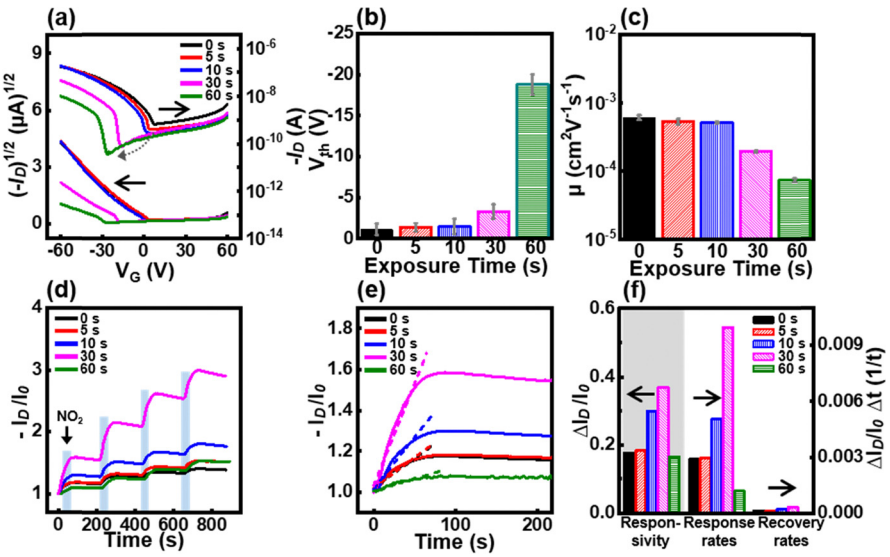

Fig. 3 (a) Transfer curve of OFET based on P3HT film with UV-O_3 treatment (plot of the drain current *vs.* gate voltage at drain voltage of −60 V). (b) Threshold voltage and (c) field-effect mobility of P3HT film with UV-O_3 treatment. (d) Repeated gas sensing curves for P3HT films with UV-O_3 treatment upon exposure to 10 ppm NO_2 followed by air. (e) Gas sensing curves at first exposure cycle. (f) Calculated gas sensing parameters, responsivity, response rate, and recovery rate upon exposure to NO_2.

by UV-O_3 treatment resulted in a decrease in field-effect mobility from 5.3×10^{-4} cm^2 V^{-1} s^{-1} to 4.1×10^{-5} cm^2 V^{-1} s^{-1} (Fig. 3c). Furthermore, UV-O_3 treatment modified the surface of the active layer, creating an oxidation layer and reducing the P3HT chain length. Various oxygen-containing functional groups were introduced by the UV-O_3 treatment. XPS analysis confirmed that the P3HT film fabricated in this study contained the highest concentration of –OH groups. These –OH groups, which are known for their unshared electron pairs, act as electron-donating groups.[41–43] When these electron-donating groups are incorporated into a p-type semiconductor, they increase the Fermi level energy, thereby reducing the hole density. The reduction in the hole carrier density induces a leftward shift in the transfer curve. Additionally, the increase in free volume hinders charge transfer, thus increasing resistance and reducing mobility.

Gas sensing performances with UV-O_3 exposure time

To examine the gas-sensing performance, the gas-sensor devices were exposed to 10 ppm NO_2 for 15 s and purged with air for 200 s. The drain current (I_D) was measured at −10 V gate voltage (V_G) and drain voltage (V_D) at various gas exposure times (Fig. 3d). The responsivity, response rate, and recovery rate were calculated as $\Delta I_D/I_0$, $\Delta R/\Delta t$, and $\Delta R/\Delta t$, respectively, from the first-exposure cycle (Fig. 3e and f). The prolonged UV-O_3 treatment time led to an increase in the current level; in particular, 30 s of treatment resulted in the highest current level. The improvement in gas-sensing performance can be attributed to the strong interaction between the oxygen functional groups and NO_2 gas molecules as well as the large free volume. The oxygen functional groups formed by UV-O_3 treatment exhibited electron-donating properties. These electron-donating groups interact with the strongly oxidizing NO_2 gas molecules, leading to an increase in the drain current. The UV-O_3 treatment reduced the P3HT chains, forming a large free volume, which increased the gas permeability of the active layer and improved the gas sensing performance.

Furthermore, the dynamic response test results of the gas sensor devices were evaluated for various harmful gases, including NO_2, SO_2, and CO_2. The source–drain current (I_D) as a function of time was recorded upon exposure to varying concentrations of these gases (10–70 ppm), as shown in Fig. 4a–c. The results demonstrated a significant increase in I_D for all gases during the exposure period (highlighted by the blue rectangular region), indicating an effective interaction between the gas molecules and the P3HT film. Among the three gases, the sensor exhibited the highest sensitivity for NO_2 with a pronounced

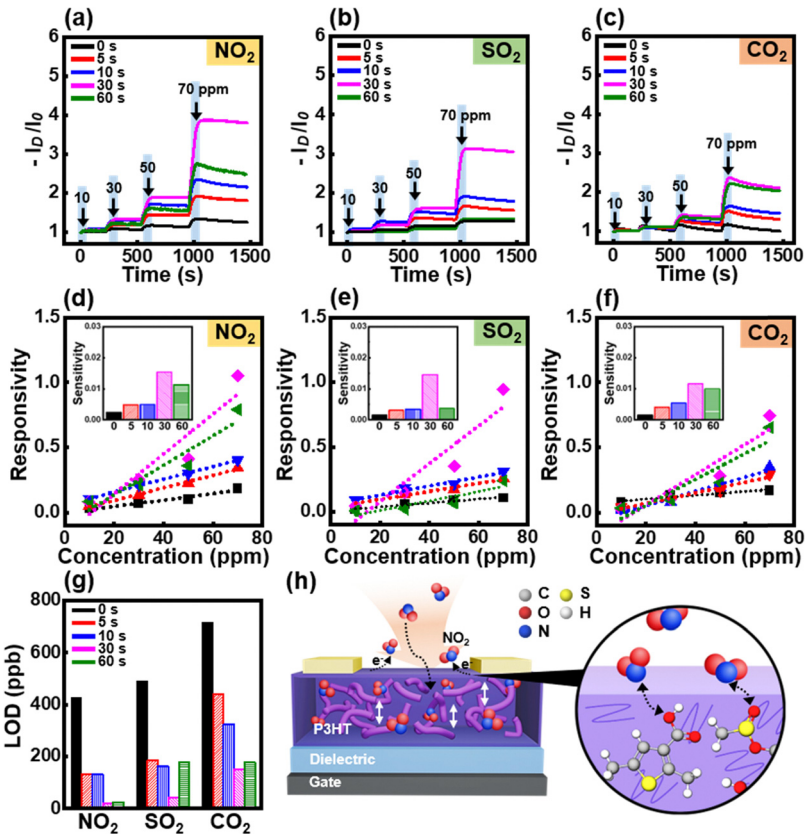

Fig. 4 Source–drain current (I_D) *vs.* time curve of OFET gas sensors based on P3HT thin films when the sensors were exposed to various concentrations of (a) NO_2, (b) SO_2, and (c) CO_2 from 10 to 70 ppm. The blue rectangular region denotes exposure time to NO_2, SO_2, and CO_2 (15 s). Linear fit shows the gas responsivity of the hybrid gas sensor devices as a function of the (d) NO_2, (e) SO_2, and (f) CO_2 concentration (the inset shows the calculated sensitivity determined from the slope of the fitted graphs). (g) Limit of detection of the gas sensor exposed to NO_2, SO_2, and CO_2. (h) Schematic of NO_2 gas adsorption in gas sensor devices employing UV-O_3 treated P3HT film.

increase in current, even at lower concentrations. These differences in the sensing performance can be attributed to the differences in the oxidation abilities of the gases. The strong oxidation property of NO_2 gas facilitates its electron-withdrawing ability, which allows it to interact more strongly with oxygenated functional groups, eliciting a more prominent response in gas-sensor devices.[44] However, the oxidation abilities of SO_2 and CO_2 gases are weaker than those of NO_2 gas, which reduces their electron-withdrawing abilities. In addition, CO_2 molecules are nonpolar, resulting in diminished interactions that significantly impair their gas-sensing abilities. In contrast, SO_2 and CO_2 induce relatively moderate changes in I_D, suggesting that the P3HT film has a higher selectivity for NO_2 detection.

The responsivity of the gas sensors was further analyzed by plotting the I_D change as a function of the gas concentration, with linear fits applied to determine the sensitivity of the devices (Fig. 4d–f). Based on the calculated sensitivities shown in the insets, the sensors exhibited a linear response to the gas concentration over the tested range. The sensor treated with UV-O_3 for 30 s displayed the highest sensitivity to NO_2 (Fig. 4d), with a gradual increase in responsivity as the UV-O_3 treatment time was prolonged to 30 s. However, a notable decline in responsivity was observed after 60 s of UV-O_3 exposure.

The limit of detection (LOD) for each gas was calculated and is summarized in Fig. 4g. With increasing UV-O_3 treatment time, the LOD for NO_2 significantly improved, reaching its lowest value after 30 s of UV-O_3 exposure.

The enhanced gas-sensing performance of the UV-O_3 treated P3HT films can be attributed to the augmented free volume and increase in the number of oxygenated functional groups, which facilitate the adsorption of gas molecules. Fig. 4h illustrates the proposed mechanism of gas adsorption on the P3HT films after UV-O_3 treatment. The untreated P3HT film exhibited minimal interaction between the gas molecules and the polymer at the surface, resulting in moderate sensor performance. After UV-O_3 treatment, the introduction of oxygenated groups augments the free volume and increases the number of interaction sites for NO_2, thereby enhancing the performance of the sensor.

Conclusions

In this study, we demonstrated that UV-O_3 treatment substantially enhanced the sensitivity of OFET-based NO_2 gas sensors. The UV-O_3 treatment oxidized and decomposed the P3HT chains, leading to an increase in the hydrophilicity and free volume within the film. These UV-O_3 treatments facilitated the introduction of oxygen-containing functional groups, which in turn improved the chemical and physical gas adsorption capabilities of the active layer. This enhanced interaction with the NO_2 molecules resulted in a notable improvement in the sensing performance. Among the gas sensor devices, the P3HT sensor treated with UV-O_3 for 30 s exhibited remarkable sensing characteristics with a sensitivity of 1.5%/ppm and an LOD value of 21.5 ppb for NO_2 gas.

This study provides a promising strategy for optimizing polymer-based gas sensors and underscores the potential of surface modification techniques for the development of high-performance environmental monitoring devices. Future studies should focus on expanding the applicability of the technique to a broad range of organic semiconductors and hybrid materials. Further investigation into optimizing the treatment parameters is necessary to enable industrial-scale implementation. These advancements will significantly enhance the performance of next-generation gas sensors, contributing to smart environmental monitoring and Internet of Things applications.

Author contributions

The manuscript was written through the contributions of all authors. All authors approved the final version of the manuscript.

Data availability

The datasets used and/or analyzed during the current study are available from the corresponding author on reasonable request. No primary research results, software or code have been included and no new data were generated or analyzed as part of this paper.

Conflicts of interest

There are no conflicts to declare.

Acknowledgements

This work was supported by the National Research Foundation of Korea (NRF) grant funded by the Korea government (MSIT) (No. NRF2023R1A2C1005218).

References

1 M. Ma, Z. Zhang, Q. Liao, F. Yi, L. Han, G. Zhang, S. Liu, X. Liao and Y. Zhang, *Nano Energy*, 2017, **32**, 389–396.
2 H. Chen, Y. Song, X. Cheng and H. Zhang, *Nano Energy*, 2019, **56**, 252–268.
3 Y. Lee, J. Kim, B. Jang, S. Kim, B. K. Sharma, J. Kim and J. Ahn, *Nano Energy*, 2019, **62**, 259–267.
4 K. Dong, Z. Wu, J. Deng, A. C. Wang, H. Zou, C. Chen, D. Hu, B. Gu, B. Sun and Z. L. Wang, *Adv. Mater.*, 2018, **30**, 1804944.
5 M. Ha, S. Lim, S. Cho, Y. Lee, S. Na, C. Baig and H. Ko, *ACS Nano*, 2018, **12**, 3964–3974.
6 C. Pang, G. Lee, T. Kim, S. M. Kim, H. N. Kim, S. Ahn and K. Suh, *Nat. Mater.*, 2012, **11**, 795–801.
7 Y. Liu, M. Pharr and G. A. Salvatore, *ACS Nano*, 2017, **11**, 9614–9635.
8 I. A. Ratiu, T. Ligor, V. Bocos-Bintintan, C. A. Mayhew and B. Buszewski, *J. Clin. Med.*, 2021, **10**, 32.
9 A. Sharma, R. Kumar and P. Varadwaj, *Mol. Diagn. Ther.*, 2023, **27**, 321–347.

10 X. Wang, L. Dong, H. Zhang, R. Yu, C. Pan and Z. L. Wang, *Adv. Sci.*, 2015, **2**, 1500169.
11 A. N. Sokolov, B. C. Tee, C. J. Bettinger, J. B. Tok and Z. Bao, *Acc. Chem. Res.*, 2012, **45**, 361–371.
12 L. Torsi, M. Magliulo, K. Manoli and G. Palazzo, *Chem. Soc. Rev.*, 2013, **42**, 8612–8628.
13 T. Cramer, A. Campana, F. Leonardi, S. Casalini, A. Kyndiah, M. Murgia and F. Biscarini, *J. Mater. Chem. B*, 2013, **1**, 3728–3741.
14 K. Baeg, M. Binda, D. Natali, M. Caironi and Y. Noh, *Adv. Mater.*, 2013, **25**, 4267–4295.
15 T. Someya, A. Dodabalapur, J. Huang, K. C. See and H. E. Katz, *Adv. Mater.*, 2010, **22**, 3799–3811.
16 X. Ren, F. Yang, X. Gao, S. Cheng, X. Zhang, H. Dong and W. Hu, *Adv. Energy Mater.*, 2018, **8**, 1801003.
17 H. Klauk, *Chem. Soc. Rev.*, 2010, **39**, 2643–2666.
18 H. Sirringhaus, *Adv. Mater.*, 2014, **26**, 1319–1335.
19 Y. Guo, G. Yu and Y. Liu, *Adv. Mater.*, 2010, **22**, 4427–4447.
20 G. Gelinck, P. Heremans, K. Nomoto and T. D. Anthopoulos, *Adv. Mater.*, 2010, **22**, 3778–3798.
21 C. Wang, H. Dong, W. Hu, Y. Liu and D. Zhu, *Chem. Rev.*, 2012, **112**, 2208–2267.
22 A. Nawaz, L. Merces, L. M. M. Ferro, P. Sonar and C. C. B. Bufon, *Adv. Mater.*, 2023, **35**, 2204804.
23 C. Zhang, P. Chen and W. Hu, *Chem. Soc. Rev.*, 2015, **44**, 2087–2107.
24 M. Hong, W. Jo, S. Jo, H. Jin, M. Kim, C. Y. Lee and Y. D. Park, *Adv. Electron. Mater.*, 2024, **10**, 2300901.
25 M. Hong, P. U. Do, C. H. Lee and Y. D. Park, *Sens. Actuators, B*, 2024, **421**, 136463.
26 Y. E. Hahm, S. Kweon, M. B. Park and Y. D. Park, *ACS Appl. Mater. Interfaces*, 2023, **15**, 7196–7203.
27 E. H. Kwon, M. Kim, C. Y. Lee, M. Kim and Y. D. Park, *ACS Appl. Mater. Interfaces*, 2022, **14**, 10637–10647.
28 J. I. Lee, M. Kim, K. C. Park, C. Y. Lee and Y. D. Park, *Mater. Chem. Phys.*, 2022, **278**, 125661.
29 D. Jang, H. Jin, M. Kim and Y. D. Park, *Chem. Eng. J.*, 2023, **473**, 145482.
30 J. R. Vig., *J. Vac. Sci. Technol., A*, 1985, **3**, 1027.
31 P. Urwyler, A. Pascual, B. Mueller and H. Schift, *J. Appl. Polym. Sci.*, 2015, **132**, 41922.
32 C. Dawo, M. A. Afroz, P. K. Iyer and H. Chaturvedi, *Sol. Energy*, 2020, **208**, 212–219.
33 L. Huang, X. Sun, C. Li, J. Xu, R. Xu, Y. Du, J. Ni, H. Cai, J. Li, Z. Hu and J. Zhang, *ACS Appl. Mater. Interfaces*, 2017, **9**, 21909–21920.
34 B. Kim, R. N. Candler, R. Melamud, M. A. Hopcroft, S. Yoneoka, H. K. Lee, M. Agarwal, S. A. Chandorkar, G. Yama and T. W. Kenny, *J. Appl. Phys.*, 2009, **105**, 013514.
35 P. J. Brown, D. S. Thomas, A. Köhler, J. S. Wilson, J. S. Kim, C. M. Ramsdale, H. Sirringhaus and R. H. Friend, *Phys. Rev. B: Condens. Matter Mater. Phys.*, 2003, **67**, 064203.
36 M. L. Chabinyc, R. A. Street and J. E. Northrup, *Appl. Phys. Lett.*, 2007, **90**, 123508.
37 C. Tengstedt, A. Kanciurzewska, M. P. de Jong, S. Braun, W. R. Salaneck and M. Fahlman, *Thin Solid Films*, 2006, **515**, 2085–2090.
38 J. Abad, N. Espinosa, R. Garcia-Valverde, J. Colchero and A. Urbina, *Sol. Energy Mater. Sol. Cells*, 2011, **95**, 1326–1332.
39 Y. Aoyama, O. Douheret, P. Leclere, D. Moerman, J. Mizukado, H. Suda, R. Lazzaroni and Y. Yoshida, *Org. Electron.*, 2017, **43**, 142–147.
40 M. Manceau, A. Rivaton, J. Gardette, S. Guillerez and N. Lemaitre, *Polym. Degrad. Stab.*, 2009, **94**, 898–907.
41 B. Petrovic, M. Gorbounov and S. M. Soltani, *Carbon Capture Sci. Technol.*, 2022, **3**, 100045.
42 Z. Zhang, J. Liu, H. Du, X. Zhao, H. Sun, M. Yang and J. Chu, *Chem. Eng. J.*, 2024, **484**, 149620.
43 J. Jia, Y. Wu, D. Zhao, B. Li, D. Wang and F. Wang, *Fuel*, 2023, **335**, 127062.
44 A. N. Kumar and K. Pal, *Mater. Adv.*, 2022, **3**, 5151–5162.